ISEM-6: Infrared Surface Emissivity Model for RTTOV-6

for the EUMETSAT NWP SAF

Vanessa Sherlock

December 1999

Satellite Applications, NWP Division, UK Meteorological Office,
London Road, Bracknell, Berks RG12 2SZ

email: vjsherlock@meto.gov.uk

1   Introduction

Accurate models of surface emissivity are required to interpret satellite radiance observations and to retrieve surface temperature. In general, emissivity will depend on satellite zenith angle and the roughness and refractive index characteristics of the surface itself. The sea surface is approximately isotropic but surface roughness due to the wind generated surface wave field must be taken into account. The land surface exhibits much greater spatial and temporal variability (e.g. soil water content, snow cover, type and senescent state of vegetation) and surface emissivity is more difficult to model as a consequence. Despite the complexity of surface emissivity specification, a very simple default infrared emissivity (unit emissivity for all satellite zenith angles and infrared wavelengths) has been used up until now in the RTTOV forward radiative transfer operator for NWP.

Over the past decade the emissivity of rough sea surface has been the subject of a number of modelling studies [1] [2] [3]. These studies, in combination with results from measurement campaigns [3] [4], suggest sea surface emissivity in the infra red can be adequately modelled. Furthermore, these models can be parameterized to run at a speed appropriate for operational (NWP) use. Improved descriptions of the infrared spectral emissivity for a range of land surface emissivity classes are also available following the study of Snyder *et al.* [5] and references therein. These studies form the basis of the new default infrared surface emissivity model introduced in RTTOV-6 (ISEM-6).

This report describes the infrared surface emissivity models implemented in RTTOV-6. Section 2 summarises the principal results from studies appearing in the literature pertaining to a physical model for the emissivity of the rough sea surface. Then, in Section 3, the implementation of the sea surface infrared emissivity model SSIREM in RTTOV-6 is described. Results from pre-operational-trial validation studies are presented and the expected impact of the parameterisation is discussed. Finally, in Section 4 modifications to the default infrared emissivities over land, snow and ice are detailed.

2 Physical model for the emissivity of the rough sea surface

The reflection coefficients for electromagnetic radiation incident on a planar boundary are described by Fresnel's equations, simplified here for the case of an air/water interface:

$$\rho_\parallel(n,\chi) = \frac{n\cos\chi - \cos\chi'}{n\cos\chi + \cos\chi'} \quad \text{and} \quad \rho_\perp(n,\chi) = \frac{\cos\chi - n\cos\chi'}{\cos\chi + n\cos\chi'} \tag{1}$$

In general, the reflectivity depends on the polarisation and the angle of incidence χ of the radiation and on the complex refractive index of water n at the wavelength of the incident radiation. Typically infra-red sensors are not polarized, and the total reflectivity is given by $\rho(n,\chi) = (\mid \rho_\parallel \mid^2 + \mid \rho_\perp \mid^2)/2$. Conservation of energy implies that the absorptance of the surface $\alpha(n,\chi) = 1 - \rho(n,\chi)$, and according to Kirchoff's law for radiance, the emissivity of the surface $\epsilon(n,\chi) = \alpha(n,\chi)$.

The sea surface is roughened by the presence of surface waves and is not planar. However, the radii of curvature of the surface waves are sufficiently large compared to the wavelengths of infra-red radiation that a tangent plane approximation[1] is valid for all sea surface roughness length scales, including capillary waves (conversely all roughness length scales contribute to surface reflectivity/emissivity). In principle then, the emissivity the rough sea surface can be determined by the integration of the Fresnel emissivity $\epsilon_F(n,\theta)$ over all facet orientations, where θ is the angle the facet normal makes with the (satellite) direction of view. This calculation, which is the basis of the Masuda model [1] and indeed all existing sea surface infra red emissivity models, requires the specification of both the complex refractive index of sea water and a statistical model for the distribution of facet slopes. The distribution of facet slopes is usually modelled, based on the measurements of Cox and Munk [6], by an isotropic Gaussian distribution with a slope variance which varies linearly with wind speed. In the paragraphs which follow we describe the results from modelling studies using the Hale and Querry refractive index for pure water [7] with Friedman's dissolved salt correction [8] and the Cox and Munk slope variance distribution. We then briefly discuss some points of importance which are specific to these models of refractive index and slope variance.

The main features (wavenumber, zenith angle and windspeed dependence) of the Masuda emissivity calculation are illustrated in Figure 1. The wavenumber and zenith angle dependence at zero windspeed are illustrated in Figures 1(a) and (b) and in the solid curve of Figure 1(d). The wavenumber dependence of the sea surface emissivity essentially follows the variation of the real part of the refractive index of water (see for example Figure 2 of Downing and Williams [9]), with emissivity decreasing as the real part of the refractive index increases. The basic variation of emissivity with zenith angle is given by the Fresnel equations: total emissivity is approximately constant for $\chi \leq 40°$ and then decreases with increasing rapidity to zero at $\chi = 90°$ (ie. $d\epsilon/d\chi$ and $d^2\epsilon/d^2\chi$ are both negative). Surface roughness modifies this variation somewhat, giving a reduction in emissivity with respect to the Fresnel value for $30° < \chi < 70°$ and an increase in emissivity with respect to the Fresnel value at $\chi > 70°$ (see for example Figures 1(c) and (d)). Note also, as illustrated in Figure 1(b), that the zenith angle variation of emissivity depends on wavenumber.

The effects of surface roughness naturally increase with increasing windspeed, but their magnitude depends strongly on the zenith angle χ: in the Masuda model emissivity is approximately independent of χ and $\mid u \mid$ for $\chi \leq 30°$ and surface roughness effects are greatest at at high χ and $\mid u \mid$. In the latter case it is worth noting that for typical satellite viewing geometries the zenith angle dependence of the emissivity remains the first order effect; for a zenith angle of 55° Masuda predicts that a variation of 10 m/s in windspeed gives approximately the same variation in emissivity as a 2° variation in zenith angle. However, more recent studies indicate that the wind speed dependence implied by the Masuda model is not correct.

Watts *et al.* [2] and Xu and Smith [3] have shown independently that surface reflection of surface emission (the Surface Emission Surface Reflection term, SESR) makes an important contribution to the effective emissivity of the sea surface. In particular, Xu and Smith show that the inclusion of the SESR term is necessary to account for the observed emissivity at $\chi > 70°$ and low wind speeds (see Figures 2(a) and (b)). Xu and Smith's model results then imply that the surface emissivity is approximately independent of wind speed for $\chi < 60°$ (Figure 2(c)), in agreement with conclusions of Watts *et al.* (Figures 2(d)). Thus, the Masuda windspeed dependence leads to an underestimation of the sea surface emissivity for $\mid u \mid > 5$ m/s. Note that the results of Watts *et al.* for the ATSR forward view $\chi \in [52 : 55°]$ can be interpreted in terms of a limiting case for typical operational satellite observations ($0 \leq \chi \leq 60°$) because the first and second derivatives of emissivity with repect to χ are negative over this range of zenith angles for all windspeeds.

Watts *et al.* went on to study the rough surface modification to the reflection of the downwelling atmospheric infra-red radiation as compared to the assumption of specular reflection at a planar surface[2]. As illustrated in Figure 3 for a satellite zenith angle of 55°, at moderate wind speeds the rough sea surface enhances the reflectivity for angles greater than the specular reflection angle (ie. the reflection lobe is lowered and broadened). This,

---

[1] The tangent plane approximation is also referred to as the Kirchoff method or the physical optics method.

[2] The effects of multiple surface reflection were also evaluated and found to be small: $\Delta T_b \leq 0.05$ K in even the driest atmospheres.

combined with the zenith anisotropy of the sky radiance field (in particular near horizon sky brightness) means that the specular reflection approximation tends to underestimate the upwelling radiance.

Watts *et al.* then evaluated the brightness temperature errors associated with a wind-independent emissivity specular reflection approximation (denoted CESR by Watts *et al.*) for a zenith angle $\chi = 55°$ using a set of 32 diverse atmospheric profiles. These results are reproduced in Figure 4. Although there is (partial) compensation of the errors inherent in the wind independent emissivity and specular reflection approximations, reflectivity errors dominate, and the CESR approximation leads to a slight underestimation of the outgoing longwave radiation. Mean brightness temperature differences are less than or equal to 0.15 K at all windspeeds in the three window regions considered (12, 11 and 3.7 μm). Maximum errors occur in the 12 μm band in dry atmospheres[3] at high windspeeds ($\overline{x} + \sigma = 0.3$ K for $| u | = 25$ m/s). In all cases the error inherent in this approximation is less than nominal forward model errors (of the order of 1 K). Perhaps more importantly, the brightness temperature changes associated with the change from unit emissivity to SSIREM emissivity are significantly larger than the CESR uncertainties in all channels of interest, as will be illustrated in section 3. For these reasons, the CESR ($\equiv$ Masuda at $| u |=0$) approximation has been adopted in the SSIREM in RTTOV-6. Parameterisation of the reflectivity enhancement is not straightforward, as it depends on both the surface wind speed and the transmittance of the overlying atmosphere. The parameterization method described by Watts *et al.* could be adopted if more accurate simulations were deemed necessary in the future.

All models and studies described above were based on Cox and Munk statistics for the distribution of facet slopes. The work of Apel [10] suggests the the Cox and Munk model may underestimate the slope variance associated with gravity capillary waves at windspeeds greater than $\sim$ 7 m/s (see Figure 5). If this is the case, then there is an effective non-linear contraction of the velocity scale in the plots illustrated above (this scale contraction has been added by hand in Figure 4 - see the text of Figure 5 for explaination of the scaling). In this context it should also be noted that at windspeeds ≥ 7 (10) m/s whitecaps begin to form. This is not taken into account in any of the models, but it is suggested by Watts et al. that in the infra-red the presence of whitecaps (foam) would only act to modify the slope variance. It is probably fair to say that there is considerable uncertainty surrounding slope variance estimates at high wind speeds, and that model validation through comparison with observations will be required.

The refractive index of sea water is a function of temperature, salinity, chlorinity and wavelength. The results of Masuda *et al.* reproduced in Figure 6 would indicate that the effect of dissolved salts (salinity, chlorinity) is negligible at operational satellite zenith angles: $\epsilon_{sea}/\epsilon_{pure} \leq 1.002$ ($\Delta T_b < 0.1$ K) for $\chi \leq 60°$ and for all ν. No explicit reference to the temperature dependence of the refractive index of water has been found in the literature surveyed. Presumably any dependence is weak, or it would have to be modelled for climate SST retrievals. Results from the observational campaign illustrated in Figures 2(a) and (b) also suggest that the wavelength dependence of the Friedman adjusted Hale and Querry refractive index for water used in the Masuda model may be deficient in the 830-900 cm^{-1} interval. This will probably not have a significant impact on forward model calculations for broadband radiometers, but should be borne in mind if these refractive index measurements are used in an a priori constraint (spectral dependence) for emissivity retrievals using the next generation of high resolution infrared sounders.

---

[3]The effects of surface emissivity and reflectivity on the observed outgoing longwave radiation are of course strongly dependent on the opacity of the overlying atmosphere, with maximum effect in optically thin atmospheres - dry atmospheres in the case of window channels.
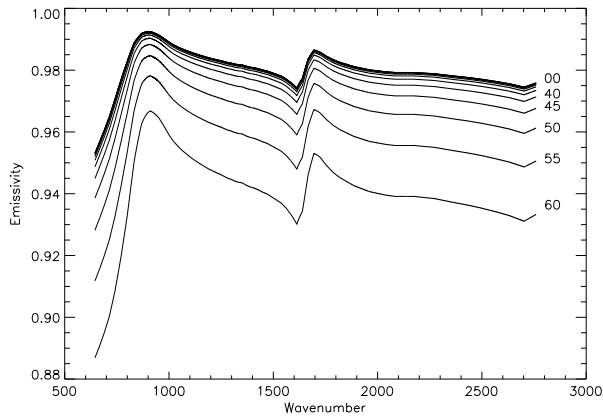
(a) Spectral and zenith angle dependence of sea surface emissivity (Masuda, $| u |$=0).
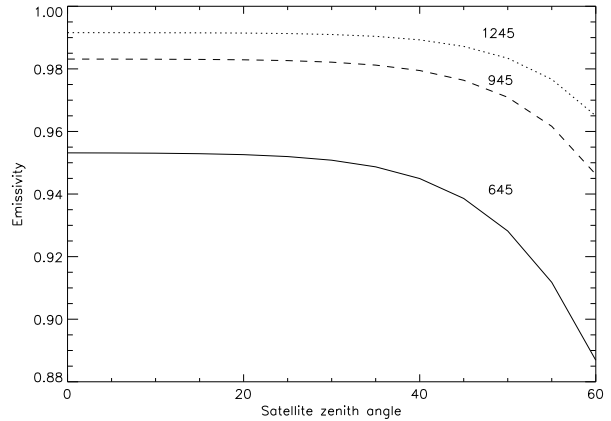
(b) Zenith angle dependence of the sea surface at 645, 945, and 1245 cm^{-1}.

(c) Windspeed dependence of sea surface emissivity for $\chi < 60°$, as predicted by Masuda (reproduced from Watts *et al.*).

(d) Windspeed dependence of sea surface emissivity for $\chi > 50°$, as predicted by Masuda (reproduced from Watts *et al.*).

Figure 1: Principal features (wavenumber, zenith angle and windspeed dependence) of the Masuda model for the emissivity of the rough sea surface.

4

(a) Comparison of ϵ retrieved from AERI observations and calculated using the Masuda model.

(b) Comparison of ϵ retrieved from AERI observations and calculated using the Masuda model including SESR.

(c) % difference in the effective surface emissivities $\epsilon(u = 0)$ and $\epsilon(u = 16\text{m/s})$ calculated as a function of χ and λ without and with the SESR term.

(d) Emissivity $\epsilon(\chi = 55°)$ as a function of windspeed for the three ATSR window channels calculated using the Masuda model (No SESR) and with SESR for two horizon cutoffs.

Figure 2: Windspeed dependence of the emissivity of the rough sea surface when surface reflection of surface emission (SESR) is taken into account. The results reproduced here from Xu and Smith (a-c) show that even at low windspeeds ($\sim$ 5 m/s) the SESR contribution must be taken into account in order to minimise the bias in observed-calculated emissivities at high zenith angles (see (a) and (b)). This in turn implies that emissivity is approximately independent of windspeed for $\chi < 60°$, a result found independently by Watts *et al.* (d). Thus the Masuda windspeed dependence leads to an underestimation of the sea surface emissivity for $\mid u \mid >$ 5 m/s.
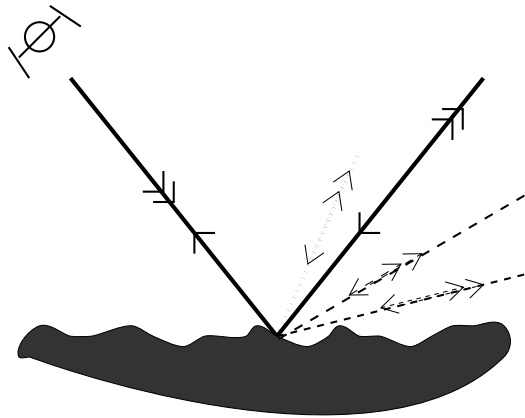
(a) Geometry of the reflectivity calculation   (b) Modification of reflectivity due to rough sea surface

Figure 3: Results from the study of Watts *et al.* concerning the reflectivity of the rough sea surface (a) and (b). Surface roughness broadens and lowers the reflection lobe (for reflection *into* the satellite field of view).

Figure 4: Brightness temperature errors associated with the CESR approximation, evaluated for the three ATSR window channels. Mean and standard deviation of ΔT_b estimated using a set of 43 diverse atmospheric profiles. Figure reproduced from Watts *et al.* The two handwritten secondary velocity scales appearing on the top x axis are illustrative of the effects of uncertainties in modelled slope variance at high wind speed (see also Figure 5 and the discussion in the main text).

Figure 5: Slope variance as a function of windspeed as deduced from observations and theoretical models, reproduced from Apel [10]. For the purposes of this discussion there are two magor points of interest (a) the slope variance predicted by a model describing the full wave spectrum including gravity-capillary waves (GCW) is $\sim 2\times$ the slope variance measurements of Cox and Munk at low windspeeds and (b) the GCW model diverges from the Cox and Munk measurements for $u > 7$ m/s, where the gravity-capillary wave contributions to the slope variance predominate. It is suggested that wavebreaking and the appearance of white caps leads to an underestimation of slope variance when using optical experimental methods (measurements of sun glint, to be precise). There are three possible scenarios (1) the measurements of Cox and Munk are representative of reality (this has been assumed in all models surveyed) (2) Cox and Munk measurements are accurate at low windspeeds - the "truth" is then given by a rescaling (by a factor 0.5) of the GCW curve or (3) the GCW curve is representative of reality. Cox and Munk predict a linear variation of slope variance with windspeed. Thus scenarios (2) and (3) lead to a non-linear contraction of the windspeed scale in the plots discussed above. Windspeed scales corresponding to scenarios (2) and (3) have been added by hand to the plot of CESR errors reproduced from Watts *et al.* in Figure 4.

Figure 6: Quantification of the effects of salinity and chlorinity: comparison of the emissivities of pure water and sea water (salinity = 34.3 ppt, chlorinity = 19.0 ppt) and the corresponding brightness temperature differences, reproduced from Masuda.

3 Implementation of the SSIREM in RTTOV

In RTTOV if the externally specified emissivity of an infrared channel is set to zero the emissivity of the channel is set to a default value. Until now unit emissivity has been used as the default emissivity in the infrared, independent of surface type. In RTTOV-6 default emissivities are based on surface-type classification (sea/land/snow/sea ice) and the SSIREM replaces the default emissivity option over sea. In this case the default emissivity is given by the channel average emissivity of the rough sea surface for the satellite zenith angle χ and is evaluated using a parameterized version of the Masuda model at zero windspeed. This parameterization is described briefly below.

3.1 Parameterization of the SSIREM

Calculations of the sea surface emissivity at high spectral resolution (0.25 cm^{-1}) were performed using the Masuda model as coded for RTIASI by Marco Matricardi [11]. Emissivity spectra were generated for thirteen satellite zenith angles (0 to 60° in steps of 5°) and zero windspeed $\mid u \mid = 0$. The high resolution emissivity spectra were then convolved with the satellite instrument spectral response functions $I(\nu)$ for each infrared channel on the satellites NOAA 2-15, METEOSAT 5-7 and MSG 1 to determine satellite-specific channel average emissivities as a function of satellite zenith angle. For each channel the satellite zenith angle dependence of the convolved emissivity was modeled by an equation of the form:

$$\epsilon(\chi) = \epsilon_0 + \epsilon_1 . \widehat{\chi}^{N_1} + \epsilon_2 . \widehat{\chi}^{N_2} \tag{2}$$

where $\widehat{\chi}$ is the normalized satellite zenith angle $\chi/60$. (with χ in degrees)and N_1 and N_2 are integer values defining the polynomial basis functions for the regression. The polynomial basis functions were determined semi-empirically - because the zenith angle variation of emissivity depends on wavenumber (recall Figures 1(a) and (b)) it was necessary to have two sets of basis functions, one for $\overline{\nu} \leq 750$ cm^{-1} and one for $\overline{\nu} \geq 750$ cm^{-1} in order to attain a fit residual of less than 0.0002 in ϵ for all channels/wavenumbers. The coefficients ϵ_0, ϵ_1 and ϵ_2 were determined using the PV-WAVE multiple regression routine REGRESS. These regression coefficients and the N_i of the basis functions have been appended to the satellite coefficient files as a data block. The corresponding read subroutines, tovcf.f and eumcf.f, have been modified accordingly.

It should be noted that the default emissivities for all SSU channels and channels 1 and 2 of TIROS-N remain 1.0 (coefficients exist for these channels, but the predicted emissivity is equal to 1.0, independent of χ) - surface contributions are vanishingly small for these channels and no error is incurred in the unit emissivity assumption. It should also be noted that the instrument spectral response functions for the VTPR instruments on board the satellites NOAA 2-5 (1-4 in RTTOV satellite identifiers) have been assumed to be identical (ie. independent of satellite) due to the lack of knowledge of the real instrument spectral responses[4].

In terms of source code, modifications have been made to the RTTOV/RTTVI subroutines emiss.f, tovcf.f and eumcf.f and an INCLUDE file emisir.h has been created. All modifications have been made using Source Code Control System SCCS: s. and p. files are available. Tangent linear, adjoint and k-code routines remain unchanged as the prognostic equation for the sea surface emissivity is independent of the atmospheric state vector, and specifically, independent of surface wind speed.

3.2 SSIREM pre-operational trial validation results

The spectral and zenith angle dependence of the Masuda sea surface emissivity at zero windspeed illustrated in Figure 1(a) is reproduced in Figures 7(a),(c) and (d) with convolved channel emissivities $\overline{\epsilon}(\overline{\nu})$

$$\overline{\epsilon} = \frac{\int I(\nu)\epsilon(\nu)d\nu}{\int I(\nu)d\nu} \quad \text{and} \quad \overline{\nu} = \frac{\int I(\nu)\nu d\nu}{\int I(\nu)d\nu}, \tag{3}$$

overlaid. The results illustrated for NOAA-15 and channel 10 of NOAA-12 in Figure 7(a), for MSG-1 and METEOSAT-5 in Figure 7(c) and for VTPR channels 1-8 in Figure 7(d) are representative of the complete set of channel average emissivities - with the exception of the change in definition of HIRS channel 10 between NOAA 5-10 and 12 and NOAA 11, 14 and 15, filter functions only vary slightly from satellite to satellite. For the NOAA satellites, where filter functions are relatively narrow and the variation of emissivity across the filter pass band is generally monotonic $\overline{\epsilon} \simeq \epsilon(\nu = \overline{\nu})$. The METEOSAT instruments have broader filter functions and $\overline{\epsilon} \neq \epsilon(\nu = \overline{\nu})$ where there is a non-monotonic variation of emissivity over the filter band pass. This is most marked for both infrared channels on METEOSAT satellites 5-7 and MSG-1 channel 8.

The VTPR channels 7 and 15 at ~ 530 cm^{-1} lie outside the wavenumber interval modeled by the RTIASI Masuda model. The channel average emissivity has been approximated by $\epsilon(\chi, \nu = 645$cm$^{-1})$, leading to an

---

[4] Convolved emissivities for VTPR channels 1-8 and 9-16 have been determined using the noaa1.flt and noaa3.flt filter functions respectively

overestimation of the emissivity. The effects of the outgoing longwave radiation are small (negligible) for all but the driest atmospheres, and even in this case the parameterized emissivity represents a significant improvement over the χ independent unit emissivity assumption. Extrapolation of emissivity values for $\nu > 2760$ cm^{-1} was also required for channel 8 of MSG 1. However, given the ISRF function for this channel tends rapidly to zero for $\nu > 2775$ cm^{-1}, the error incurred is negligible.

Convolved channel emissivities and the associated regression curves are plotted as a function of χ for HIRS channels 1, 8 and 11 in Figure 7(b). Regression fitting residuals are illustrated as a function of χ for the three channels in the lower panel of Figure 7(b) and as a function of $\overline{\nu}$ in the lower panels of Figures 7(a),(c) and (d). In all cases the absolute error in parameterised emissivity is less than 0.0002. The corresponding worst case error in brightness temperature (transparent atmosphere) is ≤ 0.02 K - an order of magnitude less than errors inherant in the CESR approximation.

In order to give a quantitative measure of the impact of the new parameterisation, forward model calculations were performed using the previous unit emissivity default and the new SSIREM defaults for $\chi \in [0 : 60^\circ]$ for a tropical atmosphere and an arctic atmosphere. The brightness temperature differences $T_b(\epsilon = 1.0) - T_b(\epsilon(\nu, \chi))$ were then evaluated. Results for NOAA-15 and channel 10 of NOAA 12, MSG-1 and METEOSAT-5 and VTPR channels 1-8 are illustrated in Figures 8 - 10. Representative values for CESR errors are also indicated for reference. They are as follows:

- CESR-A = 0.1 K is an upper bound for $\overline{\Delta T_b} + \sigma$ for all ATSR wavelengths at windspeeds less than 10 m/s. It is also the upper bound for $\overline{\Delta T_b}$ for all ATSR wavelengths except the 12 μm channel for windspeeds less than 25 m/s. We can (justifiably) assume that CESR errors less than $\overline{\Delta T_b}$ are associated with optically opaque atmospheric conditions (high water vapour contents) and those greater than $\overline{\Delta T_b}$ are associated with optically thin atmospheric conditions. Thus CESR-A provides an upper bound for CESR uncertainties for all atmospheric/simulation conditions where surface windspeeds are less than 10 m/s and for the tropical atmosphere simulations in all but the 12 μm band for windspeeds less than 25 m/s.

- CESR-B = 0.15 K is an upper bound for $\overline{\Delta T_b}$ for all windspeeds less than 25 m/s and for $\overline{\Delta T_b} + \sigma$ for all windspeeds less than 25 m/s and wavelengths except 12 μm. Thus CESR uncertainties are less than 0.15 K for all but the highest windspeeds in optically thin atmospheric conditions.

- Finally, CESR-C = 0.3 K is the upper bound for $\overline{\Delta T_b} + \sigma$ in dry atmospheres and high windspeeds ($\mid u \mid >$ 10 m/s).

In the discussions which follow the atmosphere-dependent CESR uncertainties are compared with the brightness temperature differences associated with the modified emissivity defaults in order to give a measure of significance for the predicted brightness temperature changes.

For the tropical atmosphere the only significant brightness temperature changes occur for channels with $\overline{\nu} > 2400$ cm^{-1}, and for MSG-1 channel 4. Brightness temperature changes are significantly larger for the arctic atmosphere in all window channels, particularly at large satellite zenith angles. Note that where brightness temperature differences are significant (> 0.15 K), these differences increase with increasing satellite zenith angle. The only exception to this is VTPR channel 7 (and 15), where the surface to space transmittance and its rate of change with χ predominate (ie. the surface contributions tend to zero more rapidly than any signal due to dϵ/dχ).

Thus in HIRS channels 7-10 and 17-19, METEOSAT channel 2, MSG-1 channel 1 and channels 4-8 and VTPR channels 6-8 one would expect the unit emissivity approximation to give biases (warm) which increase poleward (ie. increase as the total column water vapour decreases) and in these dry atmospheric conditions biases are also expected to increase markedly for zenith angles greater than 40°. This is in good qualitative agreement with the latitudinal and scan dependent biases observed for the HIRS instrument on board NOAA-15 - these bias plots can be viewed at `/home/fr1200/frnz/public_html/atovs.html` in `"HIRS sumob_clear"` `"mean of observed biases biases monthly"`. Conversely, it is to be expected that the implementation of the SSIREM model will reduce latitudinal and scan dependent bias corrections in these channels. This is consistant with comments from a number of participants at the ATOVS workshop at ECMWF in November 1999 who had implemented Tom Kleespies parameterisation of the Masuda model in their operational systems. It is probably worth reiterating that at high scan angles, where emissivity differences are a maximum, the scan angle dependent brightness temperature differences are a factor of ~ 5 greater than the maximum variation brightness temperature with windspeed (0.5 K) predicted by the Masuda model - ie. the primary effect of the implementation of the full Masuda model is that of the χ dependence of the sea surface emissivity. The Masuda windspeed dependence is an *incorrect* second order effect.

Further validation of the CESR approximation through comparison with observations at high windspeed (in presence of capillary waves) would be of interest, and clearly the SSIREM must be validated by pre-operational trials. If, contrary to expectations, the SSIREM does not improve (O-B) statistics then the user can always revert to the previous default emissivity either through the external specification of the channel average emissivity, or by modification of the RTTOV-6 emissivity module.
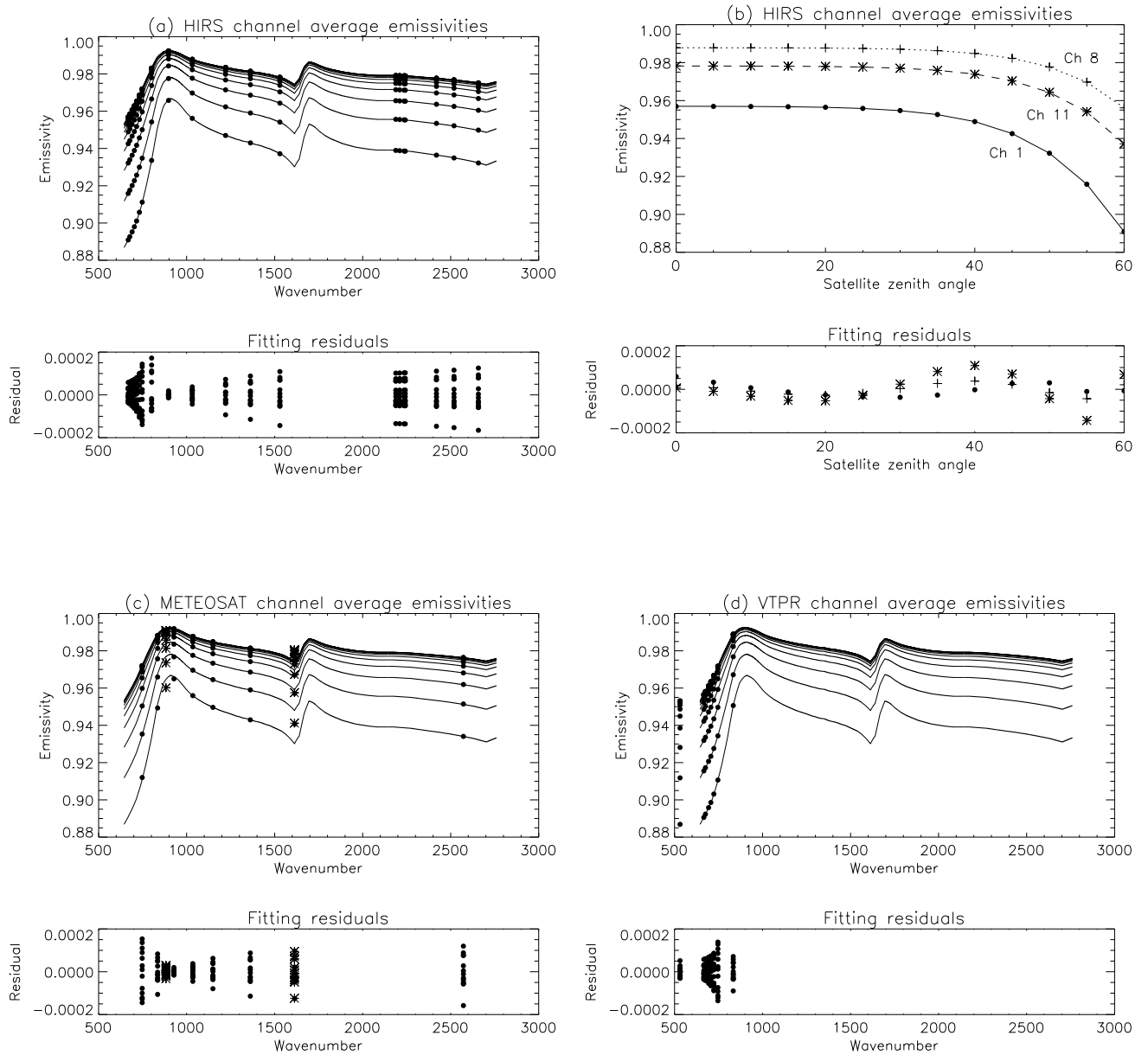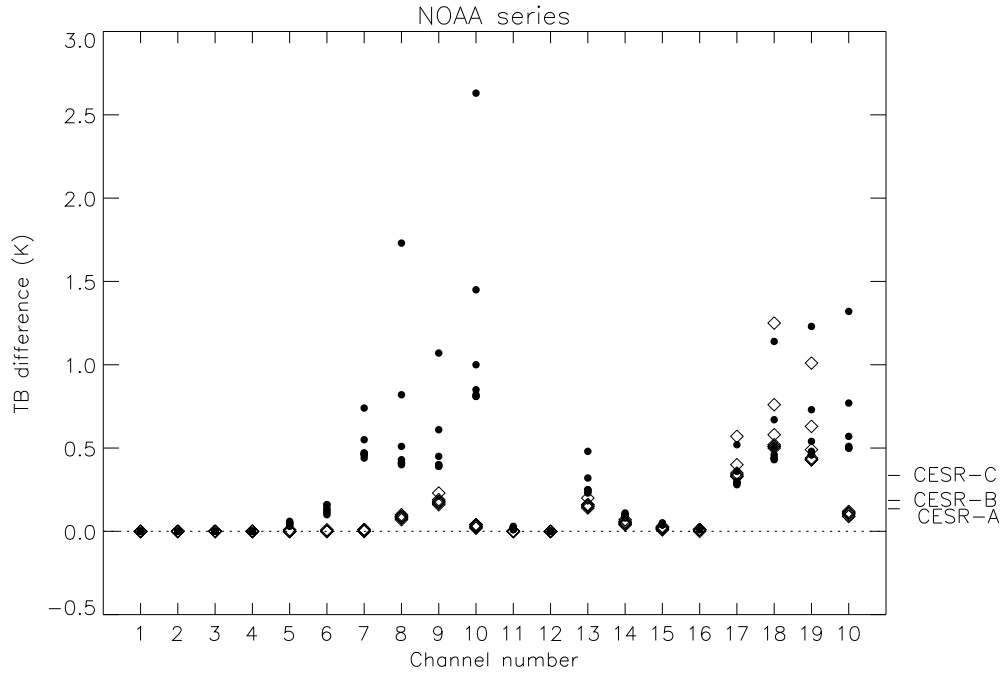
Figure 7: Representative channel average emissivities and fitting residuals plotted as a function of channel average wavenumber (a,c and d) and satellite zenith angle (b) for HIRS (NOAA-15 and HIRS channel 10 on NOAA-12), MSG-1 and METEOSAT-5 and VTPR channels 1-8.
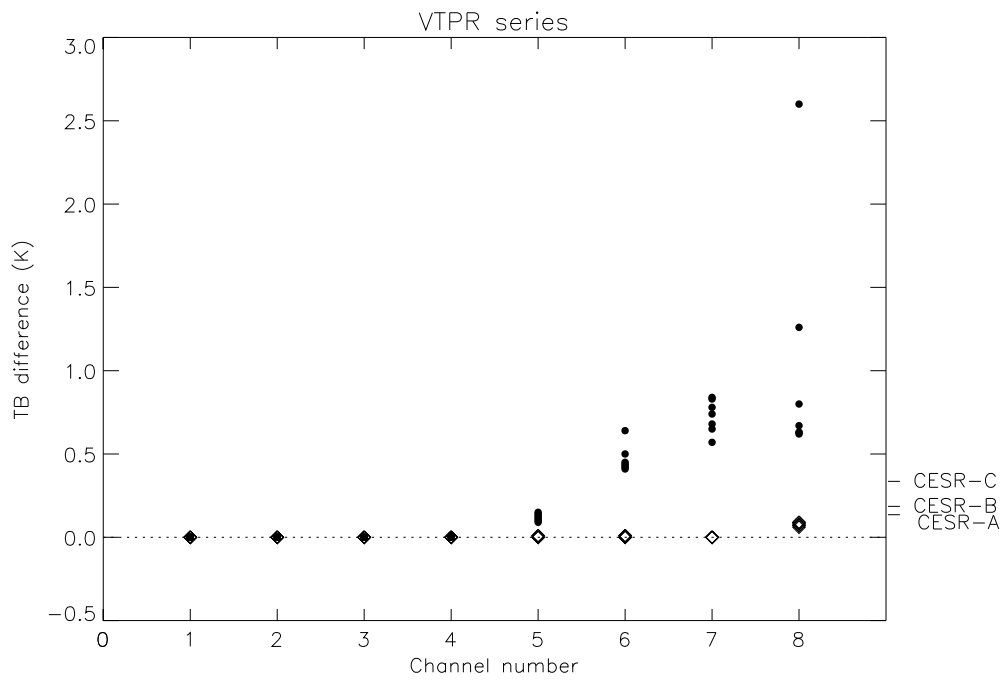
Figure 8: Brightness temperature differences TB(ϵ=1.0)-TB($\epsilon = \epsilon(\chi)$) as a function of channel number for NOAA-15 and channel 10 of NOAA-12. The corresponding channel $\overline{\nu}$ (cm^{-1}) are given in the table for reference. Simulation results for tropical and arctic profiles are illustrated with diamonds and circles respectively. Characteristic errors associated with the CESR approximation are also illustrated, and are defined as follows: CESR-A ΔT_b=0.1 K, CESR-B ΔT_b=0.15 K, CESR-C ΔT_b=0.3 K. See text for detail of the interpretation of these values.
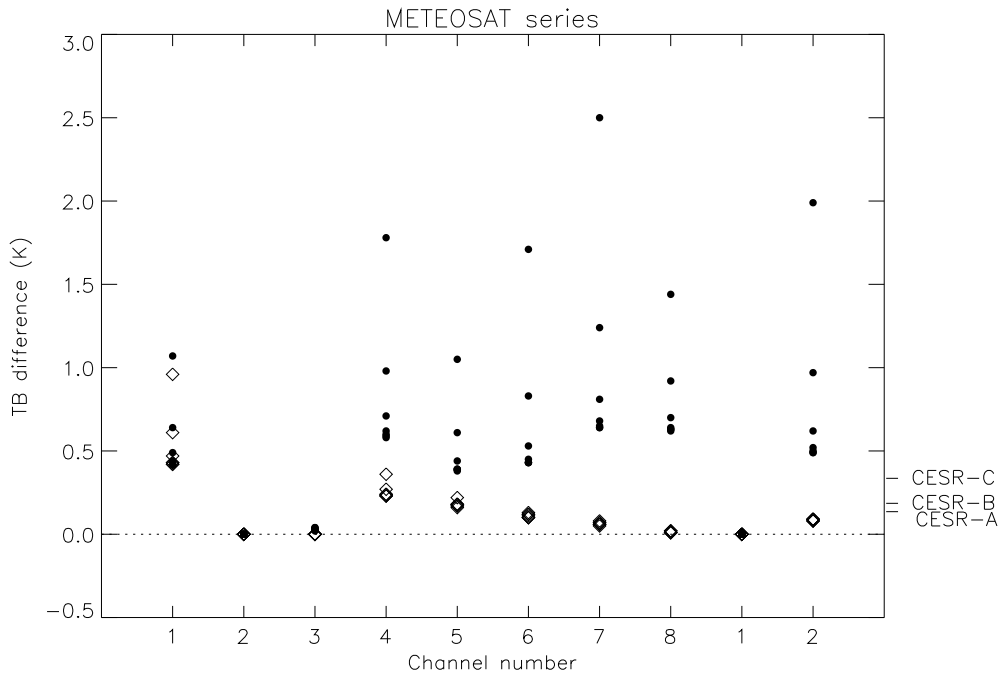
Figure 9: Brightness temperature differences TB(ϵ=1.0)-TB($\epsilon = \epsilon(\chi)$) as a function of channel number for MSG-1 and METEOSAT-5. The corresponding channel $\overline{\nu}$ (cm^{-1}) are given in the table for reference. All symbols and definitions are as given in Figure 8.

Figure 10: Brightness temperature differences TB(ϵ=1.0)-TB($\epsilon = \epsilon(\chi)$) as a function of channel number for VTPR channels 1-8. The corresponding channel $\overline{\nu}$ (cm^{-1}) are given in the table for reference. All symbols and definitions are as given in Figure 8.

4 Modification to default emissivities over land, snow and sea ice

Because of the high spatial and temporal variabilty of land surface characteristics, modelling land surface emissivity is generally a more difficult problem than the determination of the rough sea surface emissivity. Land surface emissivity will depend on satellite zenith angle, on the water content, the chemical composition, the roughness and the structure of the land surface and on vegetation type, density and state of growth.

No attempt has been made to treat the land surface emissivity in detail in RTTOV-6, but we have sought a more realistic value than unit emissivity for the default values over land, snow and sea ice. The choice of emissivity defaults was based on the work of Snyder *et al.* [5] and are as follows:

- Surface type = 0 (land), ϵ=0.98 independent of ν and χ

- Surface type = 2 (sea ice or snow), ϵ=0.99 independent of ν and χ.

These emissivity values represent a best guess emissivity for $\nu < 1750$ cm^{-1} (this wavelength interval was prioritised because in practice contributions from reflected solar radiation limit the use of channels in the 3.7 μm window region), but even a quick look at the results of Snyder *et al.* for various land surface types (reproduced in Figure 11 for convenience) suffices to give an indication of the crudeness of the approximation. Note the wavelength dependence of the land surface emissivity, the bimodal nature of the distribution of land surface emissivity in a global sense (distinct modes are associated with the green and senescent vegetation classes) and the dispersion (magnitude and skew) of emissivity within classes.

The assumption of a χ independent surface emissivity may also be a significant source of error. Reflection from ice surfaces should be well described by a rough surface specular reflection model (as used above for the sea surface) implying that $\epsilon \equiv \epsilon(\chi)$. Snow is usually described by a volume scattering model (ϵ independent of χ), however recent studies [12][13] would indicate that the emissivity of the snow surface also depends on χ. Angular dependencies should also be taken into account over smooth bare terrain (soil, sand) and in the case of sparse vegetation where the apparant fractional vegetation cover will also be a function of satellite zenith angle.

The results for the nadir view brightness temperature differences in Figures 8, 9 and 10 can be used to gauge the impact of the change to the default emissivities over land. The nadir brightness temperature differences provide an upper bound for differences at $\chi > 0°$ because as χ increases the increasing opacity of the atmosphere along the line of sight tends to reduce the surface contribution to the observed radiance i.e. the brightness temperature differences ($\epsilon \equiv 1.0$ cf $\epsilon < 1.0$) tend to zero. Thus even this simple modification to surface emissivity should make a significant impact (0.3 to 0.5 K) to the bias correction of HIRS channels 7-10 and 17-19, METEOSAT channel 2, MSG-1 channel 1 and channels 4-8 and VTPR channels 6-8 and 14-16 for climatologically dry atmospheres if infrared observations are used over land.

(a) Green broadleaf

(b) Senescent broadleaf

(c) Arid bare soil

Green sparse shrubs (d)

(e) Ice and snow

(f) Emissivity variability in MODIS band 31

Figure 11: Land surface emissivity: selected results from Snyder *et al.*. (a)-(d) Examples of the marked variabilty in land surface emissivity with vegetation cover and senescent state. (e) The spectral emissivity of ice and snow. (f) Box plots for the ranges of emisivity within the given land surface classes for MODIS band 31 (10.8-11.3 μm).

5 Conclusions

A survey of rough sea surface emissivity models appearing in the literature has been undertaken. Based on published results the Masuda sea surface emissivity model at zero windspeed has been adopted to replace the previous infrared surface emissivity default over sea. The assumptions of a windspeed independent emissivity and specular reflection lead to an underestimation, albeit small, of the upwelling longwave radiation; brightness temperature errors are less than 0.15 K in all but the driest atmospheres at high windspeeds. The satellite zenith angle dependence of the rough sea surface channel average emissivity has been parameterised for all infrared channels on the NOAA 1-15, METEOSAT 5-7 and MSG 1 satellites. Pre-operational trial results indicate that the new sea surface emissivity parameterisation should significantly reduce latitudinal and scan angle dependent bias corrections.

The values of the default infrared emissivity over land and over snow and sea ice have also been revised based on studies appearing in the literature ($\epsilon = 1.0 \rightarrow 0.98$ and 0.99 respectively). While no attempt is made to model the real spatial and temporal variability of the land surface emissivity, these revised default values should also reduce the magnitude of bias corrections in cases where infrared satellite observations are used over land. A more accurate model of land surface emissivity at infrared wavelengths could be pursued in the future.

References

[1] K. Masuda, T. Takashima, and Y. Takayama. Emissivity of pure and sea waters for the model sea surface in the infrared window regions. *Rem. Sens. Env.*, 24:313–329, 1988.

[2] P. D. Watts, M. R. Allen, and T. J. Nightingale. Wind speed effects on sea surface emission and reflection for the along track scanning radiometer. *J. Atm. Oc. Tech.*, 13:126–141, 1996.

[3] X. Wu and W. L. Smith. Emissivity of rough sea surface for 8-13 μm: modeling and verification. *Appl. Optics*, 36(12):2609–2619, 1997.

[4] W. L. Smith, R. O. Knuteson, H. E. Revercomb, W. Feltz, H. B. Howell, W. P. Menzel, N. R. Nalli, O. Brown, J. Brown, P. Minnett, and W. McKeown. Observations of the infrared radiative properties of the ocean-implications for the measurement of sea surface temperature via satellite remote sensing. *Bull. Am. Met. Soc.*, 77(1):41–51, 1996.

[5] W. C. Snyder, Z. Wan, Y. Zhang, and Y.-Z. Feng. Classification-based emissivity for land surface temperature measurement from space. *Int. J. Rem. Sens.*, 19(14):2753–2774, 1998.

[6] C. Cox and W. Munk. Measurements of the roughness of the sea surface from photographs of the sun's glitter. *J. Opt. Soc. Am.*, 44:838–850, 1954.

[7] G. M. Hale and M. R. Querry. Optical constants of water in the 200 nm to 200 μm region. *Appl. Optics*, 12:555–563, 1973.

[8] D. Friedman. Infrared characteristics of ocean water (1.5-15 μm). *Appl. Optics*, 8:2073–2078, 1969.

[9] H. D. Downing and D. Williams. Optical constants of water in the infrared. *J. Geo. Res.*, 80(12):1656–1661, 1975.

[10] J. Apel. An improved model of the ocean surface wave vector spectrum and its effects on radar backscatter. *J. Geo. Res.*, 99(C8):16269–16291, 1994.

[11] M. Matricardi and R. W. Saunders. Fast radiative transfer model for simulation of infrared atmospheric sounding interferometer radiances. *Appl. Optics*, 38(27):5679–5691, 1999.

[12] J. Dozier and S. G. Warren. Effect of viewing angle on the infrared brightness temperature of snow. *Water Resources Research*, 18(5):1424–1434, 1982.

[13] J. L. Bamber and A. R. Harris. The atmospheric correction for satellite infrared radiometer data in polar regions. *Geo. Res. Lett.*, 21(19):2111–2114, 1994.